Experimental Evaluation of Flame Radiative Feedback: Methodology and Application to Opposed Flame Spread Over Coated Wires in Microgravity

Augustin Guibaud, Jean-Marie Citerne, Jean-Louis Consalvi, Osamu Fujita, Jose L Torero, Guillaume Legros

Noname manuscript No.
(will be inserted by the editor)

Experimental evaluation of flame radiative feedback:

methodology and application to opposed flame spread over coated wires in microgravity.

Augustin Guibaud · Jean-Marie Citerne · Jean-Louis Consalvi · Osamu Fujita · Jose Torero · Guillaume Legros

Received: date / Accepted: date

Abstract The objective of this work is to quantify for the first time soot-related radiative heat transfer in opposed flow flame spread in microgravity. This article presents experimental results obtained in parabolic flight facilities. A flame is established over a solid cylindrical polyethylene coated metallic wire and spreads at a steady rate, in low velocity flow conditions allowed by the absence of buoyancy. Implementing the Broadband Modulated Absorption/Emission (B-MAE) technique, the two-dimensional fields of soot volume fraction and temperature are obtained for the first time in flame spread configuration over an insulated wire in microgravity. The consistency of the results is assessed by comparing results from independent experimental runs. From these fields, radiative losses attributed to soot in the flame are computed at each location. This map of radiative losses together with the profile of the wire surface are then used as inputs to a novel ex-perimental approach that enables the assessment of soot radiative heat feedback to the wire. Results are extracted from a specific case of a flame propagating over a polyethylene coated Nickel-Chrome (NiCr) wire at nominal pressure. The oxidizer, composed of 19% oxygen and 81% nitrogen in volume is blown at opposed flow parallel to the wire at a velocity of 200 mm.s^{-1}. This new approach provides the first detailed quantitative measurements which are required to check the relevance

Augustin Guibaud
Sorbonne Université, CNRS, UMR 7190, Institut Jean Le Rond dAlembert, Paris F-75005, France
E-mail: augustin.guibaud@upmc.fr

Jean-Marie Citerne · Guillaume Legros
Sorbonne Université, CNRS, UMR 7190, Institut Jean Le Rond dAlembert, Paris F-75005, France

Jean-Louis Consalvi
Aix-Marseille Universit, CNRS, UMR 7343, IUSTI 5 rue E. Fermi, 13013 Marseille, France

Osamu Fujita
Division of Mechanical and Space Engineering, Hokkaido University, Kita13 Nishi8, Kita-ku, Sapporo, Hokkaido 060-8628, Japan

Jose Luis Torero
Department of Fire Protection Engineering, University of Maryland, College Park, MD 20742, USA

of heat transfer models under development, therefore to better understand the mechanisms driving flame spread in microgravity.

Keywords soot · microgravity · radiative heat transfer

1 Introduction

Should manned deep space exploration missions be to happen in the near future, many safety issues that are not fully addressed aboard the International Space Station must be solved [1–3]. As astronauts will be confined for a long duration in an environment with very limited resources, there is a crucial need to prevent any damage to the structure by an accidental event such as a fire. This requires the careful development of material and procedures to minimize the risk of a fire [4]. As a result, fundamental understanding of the heat and mass transfer processes that drive ignition and flame spread in microgravity is required to reduce a lengthy and costly systematic characterization of material flammability in microgravity [5]. Modelling flame spread over a solid sample in microgravity is still a debated research topic [6]. In the past decades, different heat balance equations have been suggested to account for experimental observations. Nevertheless, there is still no consensus on the dominant modes of heat transfer, in particular at the limit states. Because buoyancy forces disappear, hypotheses deemed valid on earth may not be relevant any more in microgravity, and new arguments must be put forward. Validation of these new arguments requires access to more detailed experimental data.

It has been shown that under microgravity and low characteristic forced velocities conditions, the absence of natural convection allows to dramatically expand the time scales associated with transport and combustion processes, which may lead to an increase in both soot concentration [7] and the relative contribution to heat transfer by radiative emissions, especially from the soot continuum [8]. As the transport processes that govern soot production are also deeply affected by the absence of buoyancy [9], a specific care is to be paid to the actual configurations of flame spreading in microgravity.

Investigating two-dimensional configuration of flame spreading steadily over solid fuel in microgravity, early models used to fully neglect the radiative contribution of soot [10]. Later on, simple models emerged, accounting for a moderate radiative feedback from all gases with the introduction of a constant radiative factor [11]. Others assumed that as the radiant flux from the flame approximately balances the surface re-radiation, and therefore can be ignored [12]. Some later models still completely ignore the radiative contribution from soot [13] due to the absence of visible evidences of soot presence in the flames investigated, or neglect it [14] based on time-scale arguments related to specific experimental conditions. Although, subsequent theoretical findings allow experimental observations to be predicted, such simple models face the lack of adequate experimental data for validation, but also may tend to limit efforts in the development of detailed numerical simulations. While this reasoning is relevant for some specific situations, new models that retain these kind of hypotheses hold to arguments that may not be valid any more [15]. To provide clarity to these arguments, the following study reports on a methodology to quantify the radiative heat transfer to the solid surface attributed to soot in an axisymmetric system.

For long, the limited experimental flame probing tools available in microgravity facilities made any accurate evaluation of radiative heat transfer in sooting flames complex and inacurate. However, a compact optical setup has been recently developed in ref. [16] to allow for the quantitative mapping of soot volume fraction, temperature and local soot-related radiative losses in axisymmetric flames, using a Broadband Modulated Absorption/Emission (B-MAE) technique. Furthering the processing of these experimental measurements, the following study reports on a methodology to quantify the radiative heat transfer attributable to soot from the flame to the solid surface in an axisymmetric configuration. The methodology is here applied to a flame spreading at a steady rate in microgravity over the polyethylene coating of a cylindrical electrical wire, such as those investigated in ref. [17] and [15]. As a result, the relevance of any modelling in a cylindrical configuration can be quantitatively assessed. Starting with an overall view of the process, the different steps required to obtain soot radiative feedback evaluation from experimental data are first introduced. The implementation of the B-MAE on board parabolic flights is then outlined and the reproducibility of the experiments is especially evidenced. Then, the calculation steps required for the radiative heat feedback evaluation are detailed. Results are finally presented to show the importance of soot radiative heat feedback in the heat transfer process from the flame to the wire within the framework of the configuration investigated. The relevance of this methodology is evidenced by comparing results with those obtained using the Finite Volume Method.

2 Processing strategy

The analysis conducted here to ultimately evaluate the radiative fluxes emitted by soot towards the polyethylene surface is illustrated in Fig. 1. To achieve this goal, a first step is to evaluate the volumetric radiative losses attributed to soot in the gas phase, and and to extract the coated wire boundaries.
For the calculation of the soot related volumetric radiative losses, the following formulation in Eq.(1) is used instead of the full radiative Transfer Equation (RTE), which requires a numerical model:

$$\nabla \cdot \mathbf{q}^R = 4\,C\,\sigma\,f_v\,T^5 \tag{1}$$

where the value of the constant (C) is $1.307 \times 10^3 m^{-1}K^{-1}$ [18], and $\sigma = 5.67 \times 10^{-8}\,m^{-2}.K^{-4}$ is the Stephan-Boltzmann constant. This form of the source term may slightly underestimate the soot radiative losses in the hottest regions [19], and supposes the flame is optically thin over distances in the order of the voxel size. However, it allows a straightforward evaluation from soot volume fraction and temperature, which are the fields obtained when implementing the B-MAE technique. As a result, this basic formulation especially enables the fully experimental methodology that is outlined in the present paper. Its relevance will further be discussed in Section 5.3.
To map both soot volume fraction and temperature within the flame, B-MAE deconvolution algorithms are implemented. To reduce experimental noise, the B-MAE technique requires the averaging of multiple images. These averages need to be obtained: the flame with backlight, backlight alone, the flame alone and

the background noise. Prior work has shown that 50 images of each suffice for an accurate average [16]. To be able to obtain these averages, the rate of flame spread needs to be constant. That way flames can be shifted by a well defined distance resulting from the product of the flame spread rate and the time interval between images. In parabolic flights, a temporary transition state exists when the flame is established in microgravity. Consequently, the first step is to verify that the flame spread reaches a steady state. If the spread rate can be considered steady over a long enough period of time, averaged frames are produced. The mean contour of the coated wire is easily detected from its shadow shown on the averaged backlighted frame (see on the left of Fig.1(a)), and B-MAE technique algorithms process both averaged backlighted and unbacklighted frames displated in Fig.1(a) to obtain mappings of soot volume fraction and temperature. These fields are then used as inputs to the computations of the field of radiative losses, using the straightforward experimental model described above. The resulting fields are shown in Fig.1(b).
A second step consists of a basic geometric technique to evaluate soot-related radiative feedback from the flame to the wire. A set of hypotheses are made to simplify the problem, and consequently compute the radiative feedback attributed to any source point. A thorough analysis of the domain is performed to make sure that most of the signal captured is analysed while removing noise-dominated source points. A convergence analysis is especially required to assess the values of the mesh grid parameters, and details are provided in Section 5.2.

3 Implementation of the B-MAE technique in parabolic flights

The B-MAE setup has been incorporated to the Detection of Ignition And Mitigation Onboard for Non-Damaged Spacecrafts (DIAMONDS) rig [17]. This especially allows the investigations on flames spreading over polyethylene coated wires on Novespace A310 ZeroG parabolic flights. Such a facility provides up to 22s of microgravity with an accuracy level of $10^{-2}g_0$, where g_0=9.81 m.s^{-2}. A combustion chamber detailed in ref. [17] is used for this purpose. The chamber enables the control of the pressure, oxygen concentration and the velocity of the flow rate surrounding the samples. Within the framework of the present study, experiments focus on the configuration of a flame spreading in an opposed oxidizer flow.

3.1 Experimental Setup

The experimental setup on board the aircraft consists of three sub-rigs that are described in ref. [17]. The central element of this setup is a cylindrical combustion chamber, shown in Fig.2, with an inner diameter of 190 mm. The gas flow is straightened at the entrance (1) of the chamber to provide a flat velocity profile around the cylindrical samples (2) located along the central axis. The flow can be generated with an oxygen concentrations ranging from 0 to 21 % in volume, a chamber pressure from 0.4 up to 1.5 bars and a velocity between 0 and 300 mm.s^{-1}. Data shown here to illustrate the procedure are obtained for an oxidizer flow of 200 mm.s^{-1} set at 19% oxygen, and 1 atm.
The sample considered is a polyethylene-coated wire. The nickel-chrome metallic

core has a 0.5 mm diameter, and the coating is 0.3 mm thick. The sample length is 150 mm. Given the duration of the microgravity period at the top of each parabola and the range of spread rate recorded in the opposed flow configuration, the sample length is more than three times the maximum propagation length expected. Consequently, border effects especially linked to heat conduction in the metallic core can be neglected. Just before the microgravity period, the sample is ignited using a hot Kanthal wire, a sequence that is shorter than 8s for the configuration studied.
As prescribed in ref. [16], images of the flame spread are then captured using a JAI AT-140CL digital tri-CCD camera (see (4) in Fig.2). A telecentric lens is mounted on the camera, to restrict the light collection to beams parallel to the optical axis. With this arrangement, the spatial resolution of the projected data is 76 μm for each spectral band and images are acquired at a rate of 39.06 fps. A LED backlight behind the samples is alternatively set on and off, hence images are recorded simultaneously with and without backlight. An alternative situation would be to record all the frames without backlight first, and then all the frames with backlight, but such strategy requires knowledge of the duration of the steady propagation prior to any parabola.

3.2 Propagation Characterization

From the frames obtained, flame spread rate and pyrolysis rate are recovered using simple visualization tools. In every propagation recorded, the ignition procedure generates a temporary transition state. The heat from the flame melts the solid polyethylene as pyrolysis happens. A liquid region forms and retracts, presumably due to surface tension, forming a droplet that recedes on the metallic core. The geometry of this droplet and the evolution of the luminous flame length are tracked to assess the steady state propagation.
Once these quantities only vary by amounts below the level of noise attributed to the acquisition setup, the flame is assumed to spread at a steady rate. Away from extinction conditions, flames that spread in an opposed flow could reach a steady propagation. However, near the extinction limits [20], instabilities with characteristic time scales much larger than the duration of the parabola have been highlighted in NASA investigations aboard the ISS [21]. As a result, only flames far from the extinction limits have been probed using this method. Under the studied conditions, steady propagation was recorded over more than 7s, as highlighted in Fig. 3, with a pyrolysis rate of 0.805 mg.s^{-1}. Running a similar experiment aboard a space station would provide longer observation time. However, the observation reported here supports the assumption of steady spread rate during the parabola.

3.3 Profile of the wire

The wire contour must be detected. Averaging 50 backlighted frame during steady propagation, such as shown in Fig.1(a), a threshold method is implemented to obtain the contour of the solid and liquid interface (see the dark part in Fig.4). Due to the pixel natural grid, the smooth contour of the liquid droplet is degraded

in pixelated steps. In order to smooth the contour obtained, a linear interpolation is implemented. It could be argued that a quadratic interpolation would fit the actual interface better. Yet with the current objective of obtaining the radiative feedback, the linear approximation already captures the topology with a precision below the noise level induced by the threshold determination.

3.4 Detailed soot related fields

For a flame that achieves a spread at a steady rate, soot volume fraction and temperature fields are obtained using the B-MAE technique as outlined and validated in ref. [16]. This technique gives access to local soot absorption to evaluate the local soot volume fraction, then compares emission signals over two different spectral ranges to obtain an auto-calibrated measurement of the local temperature. A specificity of this approach is its ability to consider reabsorption at each step of the process. It is especially relevant as light rays captured by the optical setup can cross densely sooted regions over long distances. Ignoring reabsorption leads to underestimating soot temperature [16], thus the radiative loss attributed to soot. In practice, the B-MAE technique requires four sets of images, i.e. the flame with backlight, the backlight alone, the flame alone and the background noise. 50 images featuring the flame with backlight and 50 images featuring the flame without backlight are averaged over the steady spread rate period. To sustain a precautionary approach, only propagation at steady rate that are longer than 3s are considered. Background noise and backlighted images are averaged over 50 acquisitions before the sample is ignited. Fig. 4 illustrates the fields of soot volume fraction f_v and temperature T that are recovered experimentally from a given set of images.

3.5 Reproducibility

In order to quantify the precision of the B-MAE technique in parabolic flights, the reproducibility of the results was checked by comparing results from three different runs of the same experimental conditions, as detailed in Section 3.1. Each run leads to a steady flame spread rate, with a flame front velocity of 1.07 mm.s$^{-1}\pm$ 0.01 mm.s^{-1}.
Fig. 5a illustrates the spatial distribution of soot volume fraction for each parabola. Every contour delineates the region with a soot volume fraction above 5 ppm. The distributions shown only differ by a few pixels. This underlines the high level of similarity in soot locations for these measurements. Yet, the slight difference in distribution from one measurement to another forbids a pixel by pixel comparison of soot volume fraction and temperature. As a consequence, populations of soot temperature / volume fraction measurements in the flame are compared, only for location with soot volume fraction above 5 ppm. These results are displayed in Fig. 5b. It can then be inferred that soot volume fraction is recovered with a precision of 1 ppm while temperature is assessed with a precision of 50K in order to achieve profiles overlap. For the next phase of the analysis, the dataset presenting the least g-jitters is selected, and its radiative feedback is computed as illustrated in Fig. 4. The sole purpose of the B-MAE technique here is to access soot volume fraction and temperature fields. Consequently, it would be valuable to compare these fields

with the same results obtained from different approaches such as Light Induced Incandescence, however this methodology has never been deployed in microgravity environment to the author's knowledge.

4 Radiative feedback theoretical model

The volumetric radiative losses attributed to soot, i.e. the divergence of the radiative flux, at every location where soot volume fraction and temperature are measured is then computed using Eq.(1), as shown on the rightmost field in Fig. 4. This section now presents the model and the associated computations implemented to evaluates the heat feedback to the wire due to the soot radiative heat losses in the flame.

4.1 Hypotheses

The novelty of this study is to propose a rather straightforward way to compute soot related radiative heat feedback from experimental flame radiative losses and wire topology data fields.
To simplify the model, the following hypotheses are made and addressed as follows:

1. The system is axisymmetric, which is relevant in the present case of a laminar flame established over an electric wire. It is worth reminding that the flow direction, i.e. parallel the wire's axis, does not alter the symmetry of the configuration.
2. The flame is spatially divided over a regular axisymmetric mesh using a regular grid, and each voxel thus formed radiates as an independent heat source. As long as the grid dimensions remain large as compared to the characteristic lengths of the soot particles, this can be deemed valid.
3. Each source point radiates isotropically following a black body emission law, due to soot size and condensed matter considerations.
4. Light propagates in straight lines. The index may vary a little due to the differences in temperature and composition, but given the short distances considered the curvature of the light beams is ignored.
5. Re-absorption by the participating medium met by any ray along its pathway is ignored in the following. This hypothesis is not always valid when considering flames in microgravity, due to the high level of soot production observed in some configuration. This hypothesis was not adopted within the framework of the soot volume fraction and temperature measurements, because the backlight potentially crosses densely sooted regions over quite long distances. However, the absorption along the path between each source point and the wire is neglected in a first approximation because the ray path does not cross a long densely sooted region anymore. Due to the wavelength dependence of absorption, this hypothesis can hardly be addressed experimentally but is later checked using a numerical model of spatial absorption is Section 5.3.
6. All parts of the wire absorb radiations with an efficiency of 1. The full analysis is performed assuming a perfectly dark material, but the solution provided here can easily be adapted to other situations by multiplying the results by a surface absorption coefficient ϵ.

4.2 Geometry

It is important to stress here the geometry considered and its subsequent meshing. Because the wire and the flame are axisymmetric, a system of cylindrical coordinates in a referential $R_{wire}(r_w, \alpha, z)$ is set. The axis of the wire is referred to as (Oz), and its origin is the points of contact between the metallic core and the receding bulb. From symmetry considerations, only the radiative source located on the half-plane $\alpha = 0$ are considered, with an intensity integrated along α. Because of the axisymmetry again, the radiative feedback is only evaluated for $\alpha \in [0, \pi]$ and results are then transposed to $\alpha \in [-\pi, 0]$. Computation for each source point being independent, only a single source point of position $S(r_s, 0, z_s)$ is considered from now on. A system of spherical coordinates in a referential $R_{source}(r_s, \theta, \phi)$ centred on this source point is used, with angles defined as shown in Fig.6. Starting from experimental data, this system is naturally meshed on the pixel grid. Consequently, soot related radiative heat received by the wire is resolved spatially along the (Oz) axis. This is particularly relevant as heat transfer in the wire is ignored so far, so the overall heat received has no physical meaning.
The view factor computations outlined below is independent of the scale used, as long as length ratios are maintained. Arbitrary length units will be therefore adopted in the next computational phases.

4.3 Source points domain of integration

Source points are obtained from experimental measurements. Thus, they exhibit a certain level of noise. In order to limit any aberration in the radiative feedback evaluation, a threshold method is implemented on the source terms. The threshold does not rely directly on the soot volume fraction or temperature uncertainty highlighted in Section 3.5 for the following reason. If soot is wrongly detected at a given location from extinction, the second step of the B-MAE processing leads to a temperature so low that the local radiative loss at this location is close to zero. The uncertainty lies within points of weak radiative emission for which soot volume fraction or temperature is overestimated. The consequences can be particularly misleading for source points close to the wire axis: their proximity to the wire surface results in a large view factor. From the radiative loss topology displayed in Fig. 4, it can be expected that most of the radiative loss occurs in a well-delimited region of confidence. Consequently, a radiative threshold value is computed, such that 99 % of the total radiative loss is retained. In the present case, the radiative loss threshold is set at 1.79 $\mathrm{MW.m^{-3}}$.

4.4 Wire integration length

For each source point considered, the total length L_{wire} of wire to consider for the estimation of the view factor has to be specified. On the one hand, underestimating L_{wire} leads to underestimating radiative feedback to the wire. On the other hand, overestimating the domain size means longer computational time is required. Surface elements of the wire far away from the flame receive little energy, as the view factor decreases. The proper value for L_{wire} is found by working on

a simpler case of a wire of constant radius r. The view factor of such a wire seen from a distance D_S normal to the wire axis can be theoretically evaluated:

$$\Omega_{wire} = 2 \times cos^{-1}\left(\frac{r}{D}\right) \tag{2}$$

L_{wire} is then defined as the minimum length required to recover 99.9% of the theoretical view factor of a wire of radius equal to the coated wire radius, for a single source point located anywhere in the source points domain. An example is illustrated in Fig. 7. It highlights the fact that view factor integral precision varies with both cylinder radius and distance of the source point considered to the axis. In the case of a source point located at a distance $D_S = 50$ and a cylinder of constant radius $r = 25$, it highlights the necessity to consider a wire of length $L_{wire} > 4000$.

4.5 View factor evaluation

Each source point S radiates isotropically. Hence the problem is now to compute the view factor of the wire Ω_S from a given source position S.

$$\Omega_S = \iint sin(\phi) d\phi d\theta \tag{3}$$

As stated before, the view factor is not computed for the whole wire at once, but for wire surface elements. A wire surface element dS between the heights z and $z + dz$ is considered. Given geometrical properties, dS is preferentially defined in R_{wire}. However, the integral in Eq.(3) is naturally computed in the spherical coordinates defined in the R_{source} referential. From these statements, it is clear that a mandatory step is to transpose coordinates between R_{wire} and R_{source}. This is possible as the bijection between these two physical referential is obvious. To transfer variables from (θ, ϕ) to (α, Z_A), the jacobian $J = |\frac{\partial\theta}{\partial Z_A}\frac{\partial\phi}{\partial\alpha} - \frac{\partial\phi}{\partial Z_A}\frac{\partial\theta}{\partial\alpha}|$ is evaluated. The following equations heavily rely on notations adopted in Fig.6. From geometric considerations in the OSB triangle, the following equations can be inferred:

$$BS \times sin\,\theta = r(Z_A) \times sin\,\alpha \tag{4a}$$

$$BS \times cos\,\theta + r(Z_A) \times cos\,\alpha = D_S \tag{4b}$$

$$BS^2 = D_S^2 + r(Z_A)^2 - 2 \times D_S \times r(Z_A) \times cos\,\alpha \tag{4c}$$

Similar considerations in the SAB triangle lead to:

$$sin\,(\pi/2 - \phi) = cos\,\phi = \frac{AB}{AB^2 + BS^2} \tag{5a}$$

$$sin\,\phi = \frac{BS}{AB^2 + BS^2} \tag{5b}$$

Differentiating Eq.(4c and 4a), and using Eq.(4a) and Eq.(4b), one can obtain the following expression:

$$d\theta = \frac{D_S\,sin\,\alpha}{BS^2}\frac{dr}{dz}(Z_A)\,dZ_A + \frac{BS^2 r(Z_A) cos\,\alpha - D_S r(Z_A)^2 sin^2\,\alpha}{BS^2(D_S - r(Z_A) cos\,\alpha)}\,d\alpha \tag{6}$$

Also, differentiation of Eq.(5a) with input from Eq.(5b) leads to:

$$d\phi = \frac{1}{AB^2 + BS^2}\left(BS + \frac{AB}{BS}\left(D_S cos\,\alpha - r(Z_A)\right)\frac{dr}{dz}(Z_A)\right)dZ_A - \frac{AB}{AB^2 + BS^2}\,\frac{D_S}{BS}\,r(Z_A)\,sin\,\alpha\,d\alpha \tag{7}$$

From these last two expressions and Eq.(5b), the jacobian J can be computed, hence the solid angle Ω_S can finally be conveniently expressed in the referential R.

$$\Omega_S = \iint J \times \frac{BS}{AB^2 + BS^2}\,d\alpha\,dZ_A \tag{8}$$

4.6 Shadow of the wire

Boundaries with respect to α must be set at every Z_A position. If the wire were a cylinder of constant radius, the light beam from the source tangential to the surface satisfies the equation:

$$\alpha_{lim}(Z_A) = cos^{-1}\left(\frac{r(Z_A)}{D_S}\right) \tag{9}$$

This expression is implemented for wire elements with no radius variation between Z_S and Z_A. Given the opposed flow configuration of the flame spread, this is the case for most surface elements of the metallic core. However, when a section of variable radius is considered, this equation ignores the possibility that part of a wire could cast a shadow on the wire downstream the ray, or that the ray may access more surface facing the source point. Given the dimensions of the melted droplet visible in Fig. 6, these situations must be accounted for. Consequently, if the radius varies between a surface element $dS(R_1,\,0)$ and a source point S(D_S, Z_S), more refined computation is performed by considering the shadow cast by any wire element $dS'(R_2,\,Z_2)$ with $0 < Z_2 < Z_S$.

The shadow intersects dS only if:

$$Z_S \times \frac{R_1 - R_2}{R_1 + D_S} < Z_2 < Z_S \times \frac{R_1 + R_2}{R_1 + D_S} \tag{10}$$

In such a case, the intersection occurs at angles $(\alpha_1, -\alpha_1)$ such that

$$cos(\alpha_1) = \frac{(Z_S R_2)^2 - (D_S Z_2)^2 - R_1^2(Z_S - Z_2)^2}{2R_1 D_S Z_2(Z_S - Z_2)} \tag{11}$$

Consequently, for a given intersection situation, dS is only illuminated between the angles $-\alpha_1$ and α_1. These angles are evaluated for all radius values between the source point and a targeted surface element. Finally, the minimum value of α_1 corresponds to the maximum shadow boundaries $-\alpha_1^{min}$ and α_1^{min}.

An example is illustrated in Fig.8. It highlights the fact that the melted droplet shields the solid polyethylene coating right behind it from most of the flame direct radiations, under the assumption of full surface absorption, but also that the front of the bulb is more exposed to flame radiations due to the increase in diameter. Locally, the resulting profile is incorrect because the linear wire profile experimentally recovered in Section 3.3 displays sharp edges and flat sections. However, this method provides correct global estimation, and this profile is smoothed.

5 Results and discussion

5.1 Radiative heat feedback

Soot related radiative heat feedback profile is presented in Fig. 9. Raw feedback profile displays local maxima at each wire position where the radius increases. As stated before, this is a consequence of the linear interpolation model adopted for the wire surface definition. In reality, the profile should vary smoothly and so should the radiative feedback profile. This has no impact on the overall feedback assessment, but it can generate local disparities. To overcome this issue, a gaussian interpolation is performed to smooth the resulting profile. It is performed solely on the liquid droplet area, and great care is taken to ensure that the total energy is conserved. On this smoothed profile, two local maxima can be identified (see the distribution on the right in Fig. 9). The first one is on the wire metallic core, directly under the flame maximum soot radiative intensity (Z = 3.2 mm). The second one is on the side of the melted droplet facing the flame (Z = -0.4 mm). This second maxima is a consequence of the trade-off in view factor computation, as the overall wire diameter and the distance from source points of maximum intensities increase simultaneously. This highlights a specific role of the liquid droplet in the heat transfer process. Because soot re-absorption is ignored, integrating this energy feedback over the wire surface provides an upper bound of the soot related radiative feedback to the wire. In the present case, the overall soot related radiative power received by the wire is P_{soot} = 179 mW. This represents 4.9% of the total soot related radiative losses within the flame, which is 3.74 W. 10 mW is radiated onto the solid coated region, 90 mW onto the liquid droplet, and the remaining 79 mW onto the bare metallic wire. The melted region consequently harvests more than a half of the total radiative energy radiated by soot back to the wire.

P_{soot} is to be compared to a characteristic power of the complete degradation. P_0 is defined as the power required to bring the polyethylene wire coating from a solid phase at an ambient temperature of 300 K to a fully pyrolysed mixed gas phase at a temperature of 750 K. Solid LDPE has a heat capacity of 1.2 $J.K^{-1}.g^{-1}$ [22], melts at 390 K [23] with an enthalpy of fusion of 110 $J.g^{-1}$ [24], and liquid LDPE has a heat capacity of 1.6 $J.K^{-1}.g^{-1}$ [25]. LDPE pyrolysis and degradation is quite complex, given the diversity of the products released in the gas phase [26]. However, it can be assumed that it is fully pyrolyzed between 400 K and 750 K [27] before combustion events take place (even in oxidative atmosphere [28]). With a heat of decomposition of 381 $J.g^{-1}$ [29], the heat required is eventually estimated, considering that pyrolysis takes place at either 400 K or 750 K. In the present case, with a pyrolysis rate of 0.805 $mg.s^{-1}$, P_0 is equal to 1.09 W $\pm$ 0.15 W. This means that soot related radiative feedback provides between 14.5 and 19 % of the energy required to fully decompose the solid material.

5.2 Grid convergence

Mandatory discretization in Z and α requires a convergence analysis on the optimal number of grid points. Fig.10 highlights the discrepancy in results as the grid is refined in both Z and α. Starting with 1 point per pixel in Z, and 2 points in α per Z position, the grid is refined up to 100 points per pixel in Z and 100 points in α per Z position. A thinner discetization in Z leads to a reduction in shadow assessment error described in Section 4.6, and impacts the surface integration convergence. A thinner discretization in α only impacts the integration convergence. Because of the direct link to shadow assessment precision, this analysis is performed on the present geometry rather than on cylinders of constant diameter. From results shown in Fig. 10, 99% of the total energy recovered with a well refined grid (100 points per pixel in Z, and 100 points in α per Z position) is recovered using only 3 points per pixel in Z, and 4 points in α per Z position. this divides the CPU time by roughly 100 while maintaining an acceptable level of accuracy.

5.3 Optically-thin assumption

Based on the optically-thin assumption, the geometric technique introduced in this paper circumvents any complexity linked to the absorption/diffusion phenomena that can occur within the flame. Nevertheless, once the fields of soot volume fraction and temperature are obtained, the Radiative Transfer Equation (RTE) within the flame can be numerically solved. This especially allows for the computation of the incident soot-related radiative fluxes to the boundary, therefore at the wire surface. Thus, the relevance of the above methodology can be adressed by contasting it results with the outputs produced by a Finite Volume Method (FVM) that especially takes re-absorption into account through the whole process.

Here, the FVM is implemented to solve the RTE in its non-scattering formulation for the radiative intensity I_λ for axisymmetric coordinates with a 12x16 angular mesh as specified in Ref. [30]. At every location, the divergence of the radiative flux $\mathbf{q}^R$ is expressed as follows:

$$\nabla \cdot \mathbf{q}^R = \int_0^\infty \left(4\,\pi\,\kappa_\lambda\,B_\lambda - \kappa_\lambda \int_{4\,\pi} I_\lambda\,d\Omega \right) d\lambda \tag{12}$$

B_λ being the spectral blackbody radiative intensity at the local temperature T given by the Planck's law, κ_λ the local spectral absorption coefficient, and Ω the solid angle.
The Mie theory allows κ_λ to be related to f_v, assuming that soot particles are within the Rayleigh limit [16]:

$$f_v(r,z) = \frac{\lambda\,\kappa_\lambda}{6\,\pi\,E(m)} \tag{13}$$

where $E(m)$ is a function of the complex refractive index m of soot. The model predicting the spectral dependence of m_λ proposed in Ref. [31] in ethylene flames is selected here.
Among the major assumptions needed to arrive at Eq.(12), the soot scattering coefficient σ_λ is neglected as compared to its absorption one κ_λ. While this might be questionable at shorter wavelength, it is valid over the very major part of the

radiative heat transfer spectrum.

Comparisons of the two methods are displayed for the soot related radiative loss fields and radiative feedback in Figs. 11(a-c). Radiative losses are overestimated in the densely sooted regions, and underestimated near the flame front. Overall, the formulation adopted in the present paper overestimates the radiative losses related to soot by 5.7 %. Looking then at the radiative feedback to the wire, the discrepancy is of the same order of magnitude (see Fig. 11(d)). It is slightly lower on the melted droplet (5 %), as light rays cross densely sooted regions to reach the interface located away from the wire axis, thus reducing the overestimation made in the radiative loss evaluation. Consequently, it can be inferred that re-absorption can be properly ignored along the evaluation of the radiative feedback to the wire for the conditions investigated here.

5.4 Radiative feedback at normal gravity

The approach detailed above can be reproduced in normal gravity environment, for a downward spreading flame under similar inflow conditions. In such conditions, the flame reaches a steady length and spreads at a steady rate of $1.9 mm.s^{-1}$ after a few seconds. However, the molten LDPE coating keeps dripping, preventing the formation of the liquid droplet that in microgravity intercepts a large amount of the radiative energy. As the dripping material partly solidifies over the fresh coating away from the flame, it forms an eminence that breaks the axisymmetry of the system. Yet the geometry of the flame and of the wire in the vicinity of the flame is not affected, so it can be assumed that locally the axisymmetry required to perform the analysis is maintained.
Results of the B-MAE and the evaluation of the radiative feedback for the earth-bound flame are presented in Fig 12. They highlight the amplification of the role of soot radiation in microgravity (whose characteristics are specified in brackets in the following): at normal gravity, soot radiative losses in the flame add up to 0.53 W (3.74 W), the radiative heat feedback amounts to 29.7 mW on the metallic core (79 mW) and 8.9 mW on the polyethylene coated region (100 mW). Performing the analysis prescribed in section 5.1 would require estimating the pyrolysis rate from the flame spread rate. In the presence of LDPE dripping, this is not a straightforward evaluation anymore. Should we assume as an illustration a large 50% loss in dripping, this leads to a pyrolysis rate of 0.662 mg.s^{-1} hence $P_1 = 0.90 \pm 0.12$ W. In normal gravity conditions, soot related radiative feedback provides between 3.8 and 5.1 % of the energy required to fully decompose the solid material, about four times less than in microgravity. It should be noted that in this evaluation, the ratio of overall soot radiative heat feedback to soot radiative heat loss is quite similar (7.3 % versus 4.9 % in microgravity). The disappearance of the liquid droplet decreases the view factor, but it is compensated by the flame getting closer to the wire axis at earth gravity.

6 Conclusion

Reproducible conditions of flame spreading over a polyethylene coated NiCr wire in an opposed flow were investigated in parabolic flights. Implementing the B-MAE technique,

the fields of soot volume fraction, temperature, radiative heat loss and radiative heat feedback to the wire surface are successfully mapped within the spreading flame in microgravity.

Though only 5% of the overall soot related radiative losses within the flame is radiated back to the wire, it represents up to 19% of the power required to fully pyrolyze the solid LDPE coating in microgravity. This is about 4 times the value computed for a downward spreading flame propagating under similar flow conditions at earth gravity. The original methodology assembled here can be reproduced for any concurrent or opposed flame propagation in ax-isymmetric configurations. The tools are now to be deployed to assess the validity of hypotheses regarding soot related radiative feedback for any model developed to represent this configuration.

Acknowledgements The authors feel grateful to the Centre National dEtudes Spatiales for its financial support under Contract No. 130615. Osamu Fujita is supported by JAXA under the project of FLARE, a candidate experiment for the third stage use of JEM/ISS.

References

1. D.-P. Hder, M. Braun, R. Hemmersbach, Bioregenerative Life Support Systems in Space Research, Gravitational Biology, 1 113–122 (2018).
2. A. W. Kirkpatrick, C. G. Ball, M. Campbell, D. R. Williams, S. E. Parazynski, K. L. Mattox, T. J. Broderick, Severe traumatic injury during long duration spaceflight: Light years beyond ATLS, Journal of Trauma Management and Outcomes, 3 4–15 (2009).
3. V. K. Parihar, B. Allen, K. K. Tran, T. G. Macaraeg, E. M. Chu, S. F. Kwok, N. N. Chmielewski, B. M. Craver, J. E. Baulch, M. M. Acharya, F. A. Cucinotta, . L. Limoli, What happens to your brain on the way to Mars, Science Advances, (2015).
4. O. Fujita, Solid combustion research in microgravity as a basis of fire safety in space, Proceedings of the Combustion Institute, 35 2487–2502 (2015).
5. D. L. Urban, P. Ferkul, S. Olson, G. A. Ruff, J. Easton, J. S. T'ien, Y. T. Liao, C. Li, C. Fernandez-Pello, J. L. Torero, G. Legros, C. Eigenbrod, N. Smirnov, O. Fujita, S. Rouvreau, B. Toth, G. Jomaas,, Flame spread: Effects of microgravity and scale, Combustion and Flame, 199 168–182 (2019).
6. P. Kumar B, A. Kumar, A. Karpov, Near limit flame spread over thin solid fuels in a low convective microgravity environment, Proceedings of the Combustion Institute, 156 1540–7489 (2018).
7. C.M. Megaridis, B. Konsur, D.W. Griffin, Soot-field structure in laminar soot-emitting microgravity non-premixed flames, *Proc. Combust. Inst.* 26 (1996) 1291–1299.
8. W. Kong, F. Liu, Numerical study of the effects of gravity on soot formation in laminar coflow methane/air diffusion flames under different air stream velocities, *Combust. Theory Modelling* 13 (2009) 993–1023.

9. G. Legros,J.L.Torero, Phenomenological model of soot production inside a non-buoyant laminar diffusion flame, *Proc. Combust. Inst.* 35 (2015) 2545–2553.
10. S. Bhattacharjee, R.A. Altenkirch, Radiation-controlled, opposed-flow flame spread in a microgravity environment, Symposium (International) on Combustion, 23 1627–1633 (1991).
11. S. Bhattacharjee, R. Ayala, K. Wakai, S. Takahashi, Opposed-flow flame spread in microgravity-theoretical prediction of spread rate and flammability map, Proceedings of the Combustion Institute, 30 2279–2286 (2005).
12. M. Thomsen, C. Fernandez-Pello, D. L. Urban, G. A. Ruff, S. L. Olson, Upward Flame Spread over a Thin Composite Fabric: the Effect of Pressure and Microgravity, International Conference on Environmental Systems, 48 (2018).
13. S.L. Olson, F.J. Miller, S. Jahangirian, I.S. Wichman, Flame spread over thin fuels in actual and simulated microgravity conditions, Combustion and Flame, 156 1214-1226 (2009).
14. S. Bhattacharjee, M. Laue, L. Carmignani, P. Ferkul, S. Olson, Opposed-flow flame spread: A comparison of microgravity and normal gravity experiments to establish the thermal regime, Fire Safety Journal, 79 111–118 (2016).
15. M. Nagachi, F. Mitsui, J.M. Citerne, H. Dutilleul, A. Guibaud, G. Jomaas, G. Legros, N. Hashimoto, O. Fujita, Can a spreading flame over electric wire insulation in concurrent flow achieve steady propagation in microgravity?, Proceedings of the Combustion Institute, 37 1540–7489 (2018).
16. A. Guibaud, J.M. Citerne, J.M. Orlach, O. Fujita, J.L. Consalvi, J.L. Torero, G. Legros, Broadband modulated absorption/emission technique to probe sooting flames: Implementation, validation, and limitations, Proceedings of the Combustion Institute, 37 1540–7489 (2018).
17. J.M. Citerne, H Dutilleul, K Kizawa, M Nagachi, O Fujita, M. Kikuchi, G. Jomaas,S. Rouvreau, J.L. Torero, G. Legros, Fire safety in space – Investigating flame spread interaction over wires, Acta Astronautica, 126 500–509 (2016).
18. G.L. Hubbard,C.L. Tien, Infrared mean Absorption Coefficients of Luminous Flames and Smoke, Journal of Heat Transfer, 100 235–239 (1978).
19. S.J. Brookes, J.B. Moss, Predictions of Soot and Thermal Radiation Properties in Confined Turbulent Jet Diffusion Flames, Combustion and Flames, 116 486–503 (1999).
20. M. Nagachi, F. Mitsui, J.-M. Citerne, H. Dutilleul, A. Guibaud, G. Jomaas, G. Legros, N. Hashimoto, O. Fujita, Effect of Flow Direction on the Extinction Limit for Flame Spread over Wire Insulation in Microgravity International Conference on Environmental Systems, 48 (2017).
21. S.L. Olson, P.V. Ferkul, Microgravity flammability boundary for PMMA rods in axial stagnation flow: Experimental results and energy balance analyses, Combustion and Flame, 180 217–229 (2017).
22. B. Wunderlich, The ATHAS database on heat capacities of polymers, Pure App. Chem., 67 1019–1026 (1945).
23. A.S. Luyt, J.A. Molefi, H. Krump, Thermal, mechanical and electrical properties of copper powder filled low-density and linear low-density polyethylene composites, Polymer Degradation and Stability, 91 1629-1636 (2006).
24. I. Krupa, G. Mikov, A.S. Luyt, Phase change materials based on low-density polyethylene/paraffin wax blends, European Polymer Journal, 43 4695–4705 (2007).
25. Y. Jin, B. Wunderlich, Heat Capacities of Paraffins and Polyethylene, J.Phys.Chem., 95 9000–9007 (1991).
26. S. Lovett, F. Berruti, L.A. Behie, Ultrapyrolytic Upgrading of Plastic Wastes and Plastics/Heavy OilMixtures to Valuable Light Gas Products, Ind. Eng. Chem. Res. 36 4436–4444 (1997).
27. J.J. Park, K. Park, J.-W. Park, D.C. Kim, Characteristics of LDPE Pyrolysis, Chem. Eng., 19 658–662 (2002).
28. R. Sonnier, G. Dorez, H. Vahabi, C. Longuet, L. Ferry, FTIRPCFC coupling: A new method for studying the combustion of polymers, Comb. and Flame, 161 1398–1407 (2014).
29. G. Agarwal, B. Lattimer, Method for measuring the standard heat of decomposition of materials, Thermochimica Acta, 545 34–47 (2012).
30. E.H. Chui, G. D. Raithby, P. M. J. Hughes, Prediction of radiative transfer in cylindrical enclosures with the finite volume method, J. Thermophys. Heat Transf. 6 (1992) 605–611.
31. H.Chang, T.T. Charalampopoulos, Math. and Phys. Sciences 430 (1990) 577–591.

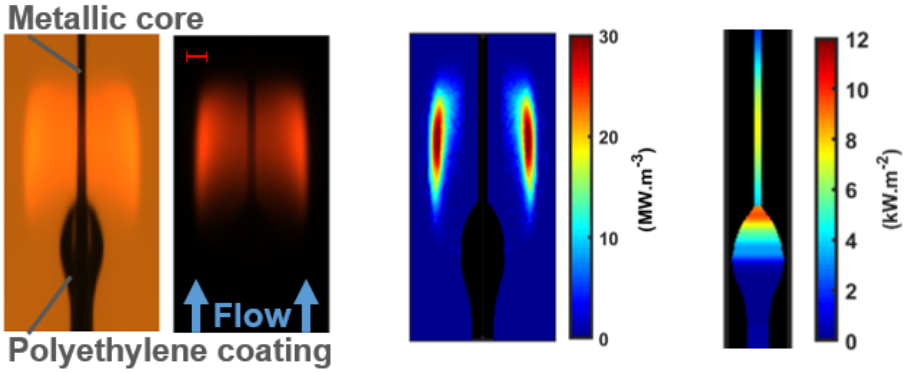

(a) (b) (c)

Fig. 1: (a) Typical frames imaging the flame spreading upstream an opposed oxidizer flow in microgravity over the polyethylene coated wire. Delivered by the B-MAE technique, these images are obtained simultaneously with (left) and without (right) backlight. The solid polyethylene is melted by the flame, forming a molten droplet that recedes on the metallic core. Oxidizer flow direction (blue) and a 1mm scale (red) are displayed (right). From these frames, the fields of soot temperature and volume fraction are retrieved using the B-MAE technique, leading to (b) the computed field of soot related radiative losses within the flame. (c) The radiative heat feedback attributed to soot from the flame to the surface of the solid and liquid phases of the wire can then be evaluated.

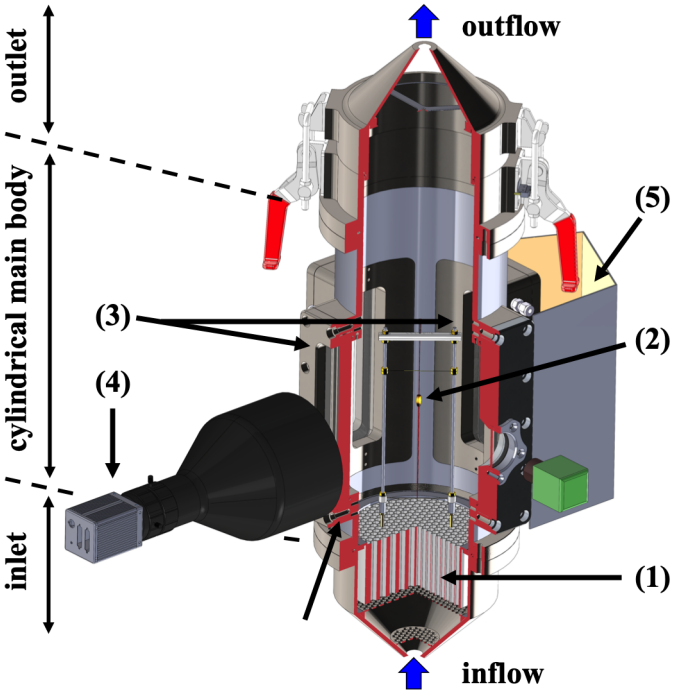

Fig. 2: Schematic view of the combustion chamber incorporated to the DIAMONDS rig: (1) honeycomb; (2) burning sample (polyethylene coated wire); (3) windows; (4) camera equipped with a telecentric lens; (5) backlighting screen illuminated by red, green, and blue LEDs. The power of every set of LEDs can be adjusted independently.

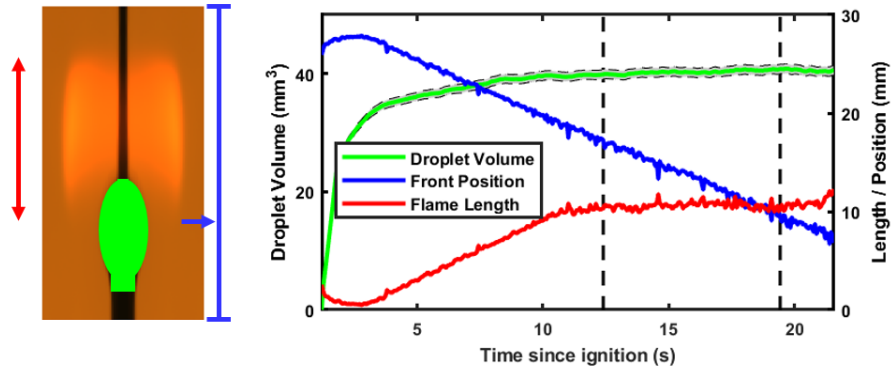

Fig. 3: Steady state is assessed in parabolic flight by tracking the evolution of the flame front position (blue), flame length (red), and liquid droplet volume (green). Between the black dotted lines, the flame length slightly oscillates around a steady value, the droplet volume does not appreciably change and the flame front moves linearly: the flame is assumed to spread at a steady rate.

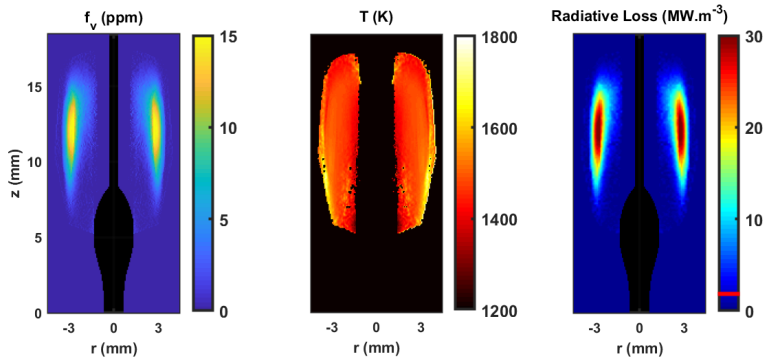

Fig. 4: Soot volume fraction, temperature and radiative losses fields obtained in microgravity from the B-MAE technique. Shadow of the condensed fuel phases reveals in black. Temperature and hence radiative losses are only evaluated over positions where soot volume fraction levels are above the background noise. In the radiative feedback evaluation, only source points with radiative losses above the threshold level, displayed in red on the scale (1.79MW), are considered.

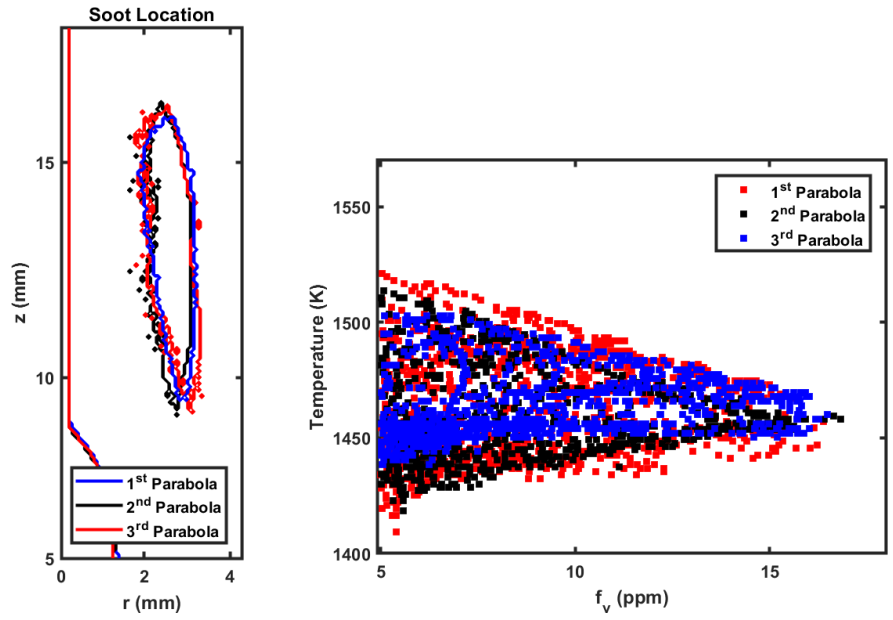

(a) (b)

Fig. 5: (a) Comparison of the spatial distributions of soot volume fraction in the flame for three different parabolas, with the same flow and sample characteristics. The contours delineate the regions with soot volume fractions above 5 ppm. The wire profiles are visible along the left vertical axis. (b) Comparison of experimental measurements in the (f_v, T) plane. From this graph, it can be assumed that the B-MAE technique recovers soot volume fraction with a precision of ± 1 ppm and temperature with a precision of ± 50K.

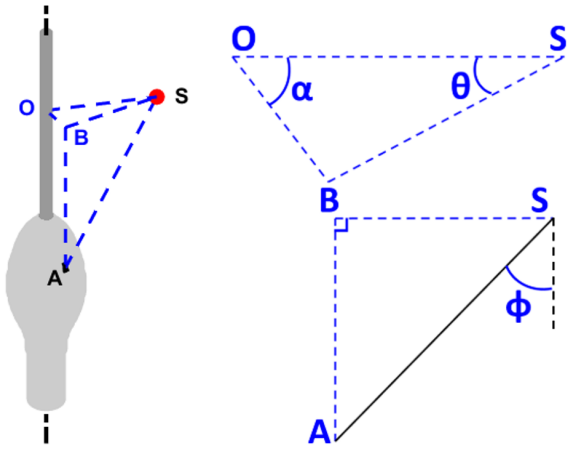

Fig. 6: Illustration of the geometry adopted. The wire coated surface is displayed in light grey, and the metallic core in dark grey. For a source point S, and a target point A, spherical coordinates in a referential $R_{source}(r_s, \theta, \phi)$ are defined. B is the projection of A on the plane that contains S and normal to the (Oz) axis. From that construction, $\theta = \widehat{OSB}$, $\phi = \frac{\pi}{2} - \widehat{BSA}$. In the referential R_{wire}, $\alpha = \widehat{SOB}$.

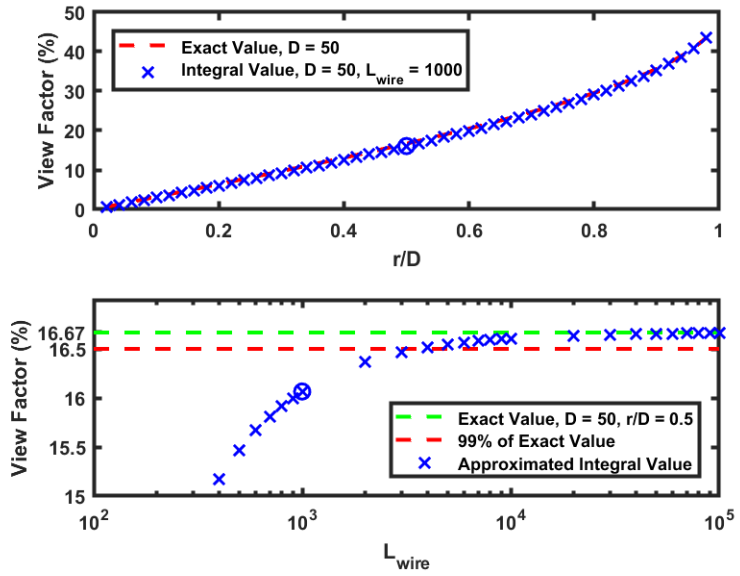

Fig. 7: Evaluation of the view factor in the case of a wire of constant radius and infinite length. The deviation of the experimental measurement depends on the distance D of the source point to the wire axis as well as the wire radius r (top). For the situation r/D = 0.5, increasing the length taken into account on each side increases the precision of the evaluation. The minimum length L_{wire}^{min} to consider is the one to recover 99% of the theoretical view factor for each source point position (bottom). The circled crosses identify the same calculation case.

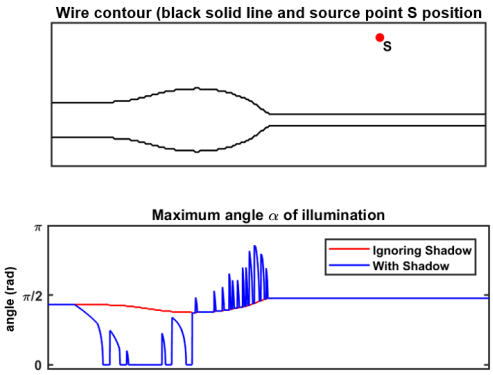

(a) Comparison of angular profiles.

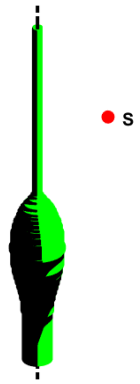

(b) Correct shadow evaluation.

Fig. 8: Evaluation of the wire view factor from a source point S. If the wire diameter changes along the wire length, a complex shadow profile evaluation must be performed taking into account the full wire profile. (a) Ignoring the real shadow profile leads to an overestimation of the visible section behind the liquid droplet, and an underestimation of the visible section at the front. (b) The surface that is visible from the source point S is coloured in green and the shadow in black.

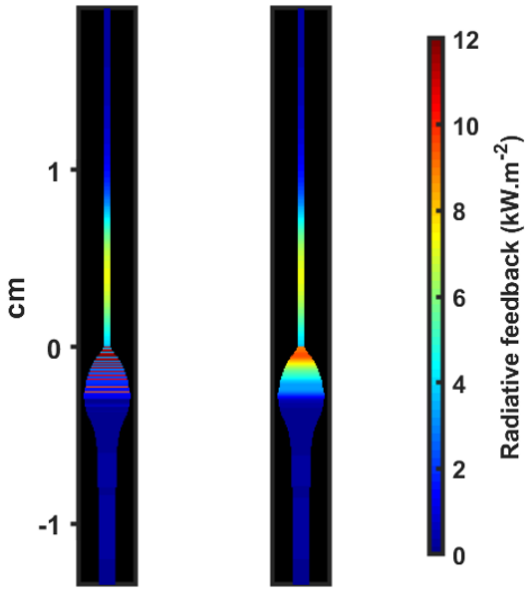

Fig. 9: Radiative feedback attributed to soot from the flame to the wire surface. The raw and smoothed outputs of the methodology are displayed on the left and on the right, respectively. The need for a smoothing process over the droplet comes from the linear extrapolation required after the numerical detection of the experimental wire contour. A local maximum is located on the metallic core directly under the flame maximum radiative losses (Z = 3.2 mm). A second local maximum appears on the side of the polyethylene bulb facing the flame (Z = -0.4 mm) as a consequence of the view factor increase.

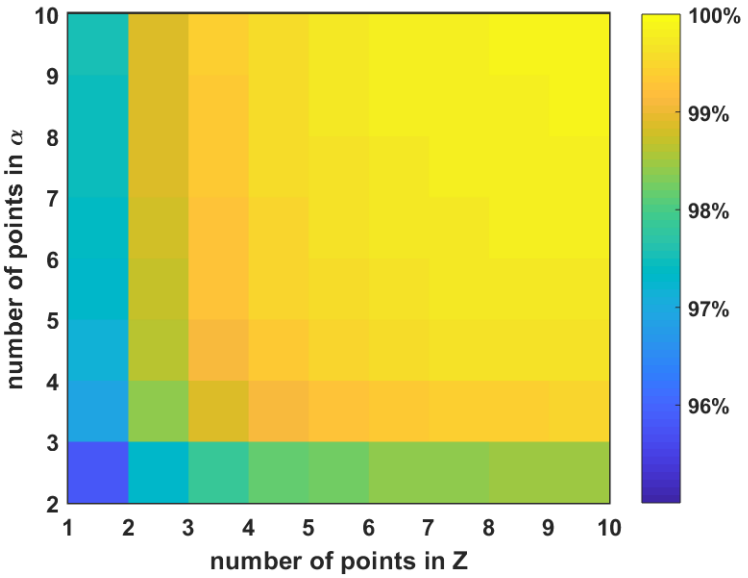

Fig. 10: Evaluation of the soot related radiative feedback integrated along the wire. 100 % corresponds to the results obtained discretizing 100 points in Z per pixel and 100 points in α per point in Z. A small number of grid points is enough to guarantee a high resolution while keeping the computational time reasonable.

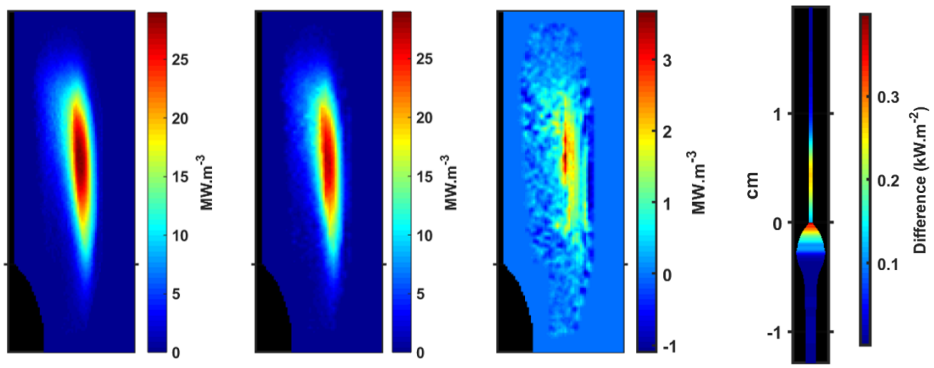

(a) $4\,C\,\sigma\,f_v\,T^5$ (b) FVM (c) = (a) - (b) (d) Feedback

Fig. 11: Soot related radiative loss within the flame obtained using (a) a direct evaluation, (b) the Finite Volume Method approach. The two methods lead to similar distributions. The difference is highlighted in (c). Further computations lead to the radiative flux distribution along the wire, like those shown in Fig. 9. (d) The resulting difference can then be evaluated.

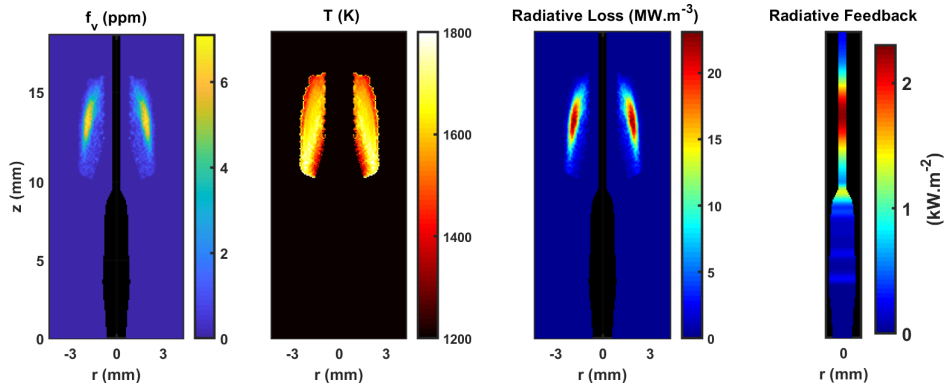

Fig. 12: B-MAE and radiative feedback evaluation for a flame propagating under similar inflow conditions at normal gravity. The visible flame is shorter, propagates faster with some dripping involved, and shows lower amounts of soot particles at a higher temperature. Overall, this contributes to weaker soot radiative heat losses in the flame, and a smaller contribution of soot radiative heat feedback to the wire surface.